ADVANCED QUANTUM TECHNOLOGIES
www.advquantumtech.com

Frequency-Dependent Squeezing via Einstein–Podolsky–Rosen Entanglement Based on Silicon Nitride Microring Resonators

*Haodong Xu, Zijun Shu, Nianqin Li, Yang Shen, Bo Ji, Yongjun Yang, Tengfei Wu, Mingliang Long, and Guangqiang He**

Considerable efforts have been devoted to augmenting the performance of displacement sensors constrained by quantum noise, particularly within high-precision applications such as gravitational wave detection. Frequency-dependent squeezing methodologies have adeptly exceeded the standard quantum limit in optomechanical force measurements, catalyzing profound advancements in the field. Concurrently, notable strides in integrated photonics have paved the way for the realization of integrated Kerr quantum frequency combs (QFCs). In this work, a sophisticated platform designed for the creation of Einstein–Podolsky–Rosen (EPR)-entangled QFCs utilizing on-chip silicon nitride microring resonators is presented. This platform facilitates an exhaustive analysis and optimization of entanglement performance, establishing a robust framework for noise mitigation. By incorporating the quantum dynamics of Kerr nonlinear microresonators, the system accommodates at least 12 continuous-variable quantum modes, including 6 pairs of concurrently EPR-entangled states. Moreover, through precise tuning of the detection angle of the idler mode, the signal mode transitions into a single-mode squeezed state. Harnessing the frequency-dependent nature of this detection angle enables the achievement of frequency-dependent squeezing. A comparative analysis under different dispersion conditions is also presented.

1. Introduction

Quantum noise constitutes a fundamental limitation in ultra-precise displacement measurements, particularly in applications such as gravitational wave detection.[1,2] It originates from vacuum fluctuations that infiltrate the interferometer through its dark readout port,[3] and is typically classified into two principal components: quantum back-action noise, which arises from photon radiation pressure, and shot noise, which emerges due to phase fluctuations. In the domain of gravitational wave detectors, shot noise manifests as phase deviations in the incoming light field, while radiation pressure noise is induced by fluctuations in the field's amplitude. The employment of squeezed light mitigates quantum noise by diminishing the uncertainty in specific quadratures of the electromagnetic field.[4–6] To counter shot noise, frequency-independent squeezing has been implemented in single quadratures at various observatories.[7,8] Optimal frequency-dependent squeezing can be realized by reflecting squeezed light through a low-loss, narrowband filter cavity.[9–11] Nevertheless, fulfilling the stringent linewidth and low-loss requirements essential for gravitational wave detection presents formidable challenges, even with ultra-high vacuum systems and state-of-the-art cavity mirrors. Specifically, achieving these requirements necessitates a filter cavity with a minimum length of 100 meters, resulting in substantial technical complexities and costs.[12] To effectively attenuate quantum back-action noise and surpass the standard quantum limit (SQL), a diverse array of quantum non-demolition measurement methodologies has been proposed, including variational readout,[9,13] stroboscopic measurements,[14,15] two-tone measurements,[16–18]

H. Xu, Z. Shu, N. Li, Y. Shen, B. Ji, G. He
State Key Laboratory of Advanced Optical Communication Systems and Networks, Department of Electronic Engineering
Shanghai Jiao Tong University
Shanghai 200240, China
E-mail: gqhe@sjtu.edu.cn

Y. Yang, T. Wu
Science and Technology on Metrology and Calibration Laboratory, Changcheng Institute of Metrology Measurement
Aviation Industry Corporation of China
Beijing 100095, China

M. Long
Shanghai Astronomical Observatory
Chinese Academy of Sciences
Shanghai 200030, China

G. He
State Key Laboratory of Precision Spectroscopy
East China Normal University
Shanghai 200062, China

The ORCID identification number(s) for the author(s) of this article can be found under https://doi.org/10.1002/qute.202400473

DOI: 10.1002/qute.202400473

and the optical spring effect.[19] In tandem with these advancements, innovative strategies have emerged for generating frequency-dependent squeezed states without reliance on external filter cavities, capitalizing on the frequency-dependent properties of EPR-entangled states to achieve optimal detuning.[20] Additional studies have demonstrated the creation of two-mode frequency-squeezed vacuum states via EPR entanglement,[21,22] with the squeezing angle meticulously controlled by an auxiliary coherent locking field.[23,24] Some approaches further exploit detuned optical parametric oscillators (OPOs) to generate frequency-dependent squeezing,[25] wherein the frequency-dependent Wigner function[26] is reconstructed through quantum tomography, revealing its rotational attributes. These methodologies have yielded promising results in reducing quantum noise. In contrast, our research focuses on silicon nitride (Si_3N_4) microring resonators to generate EPR-entangled pairs and explore frequency-dependent squeezing.

Our research leverages recent advancements in integrated photonics, particularly within the domain of quantum technologies. Notably, successful single-photon detection on Si_3N_4 platforms accentuates the potential for generating high-fidelity quantum photons.[27] Additionally, squeezed light has been realized through sub-threshold spontaneous four-wave mixing (FWM) in silicon nitride microring resonators,[28] while narrowband photon pairs have been generated in silicon-on-insulator micro-ring cavities.[29] A fully interconnected multi-user quantum network has been actualized, comprising six photon pairs.[30,31] Moreover, cutting-edge techniques for the representation and verification of multimode continuous-variable quantum states, alongside multiplexing methodologies spanning time, frequency, and spatial dimensions,[32,33] are integral for the scalable generation of entangled states. These breakthroughs, coupled with investigations into nonlinear phenomena within soliton networks and multimode lattices,[34] underscore the growing prominence of integrated Kerr quantum optical frequency combs in quantum information processing and metrology. Silicon nitride Microring Resonators mark a significant advancement over conventional OPOs based on bulk nonlinear crystals such as periodically-poled potassium titanyl phosphate.[21] Their chip-scale miniaturization, tunable dispersion, and inherent compatibility with integrated photonic platforms address key limitations of traditional free-space OPOs, offering superior scalability, efficiency, and compactness. The small waveguide cross-section facilitates the simultaneous generation of multiple two-mode squeezed states, while advanced CMOS fabrication technologies enable precise control of both coupling coefficients and dispersion properties. These features are further enhanced by the material properties of silicon nitride, including ultra-low optical loss, a broad transparency window, and seamless integration with existing CMOS infrastructure. Collectively, these attributes position silicon nitride Microring Resonators as a premier platform for investigating frequency-dependent quantum squeezing with unprecedented precision.

In this work, we introduce a sophisticated platform[35] based on integrated silicon nitride micro-ring resonators, engineered for precise dispersion and coupling control, facilitating the generation of EPR-entangled frequency combs with no fewer than 12 channels (six pairs), each capable of yielding frequency-dependent single-mode squeezed states. Furthermore, we provide an exhaustive analysis of entanglement distribution across multiple modes using bipartite entanglement criteria. Two distinct silicon nitride micro-ring cavity configurations are employed to simulate normal and anomalous dispersion conditions, respectively. Our focus is directed toward the study of frequency-dependent squeezing mediated by EPR entanglement, wherein we determine the optimal readout angles for achieving maximal squeezing at various observation frequencies. Ultimately, we delineate the intricate relationships between entanglement bandwidth, threshold power, and quality factor. This approach affords unparalleled control over quantum noise, which could significantly enhance the sensitivity of displacement measurements, such as those used in gravitational wave detectors, and holds considerable promise for expanding the utilization of fully integrated entangled resources in the realm of quantum metrology.

The organization of this paper is as follows: Section 2 provides a detailed overview of the simulation model for the integrated silicon nitride microresonator, coupled with an introduction to the principles of dispersion and coupling engineering. In Section 3, we formulate a theoretical framework for four-wave mixing within the microresonator, grounded in OPO theory, and establish the quantum entanglement criteria for signal and idler modes. This section also demonstrates the generation of single-mode squeezed states using EPR-entangled pairs. Section 4 delves into the extraction and application of critical parameters within the simulation, examining their influence on entanglement dynamics and noise suppression. A comprehensive analysis of entanglement features and frequency-dependent squeezing is presented, highlighting the distinctions between normal and anomalous dispersion. This section culminates in the presentation of correlation curves linking the intrinsic quality factor Q_0 and the loaded quality factor Q to entanglement bandwidth and threshold power. Finally, Section 5 offers a succinct summary of the research findings, including the analysis of frequency-dependent squeezing via a silicon nitride-based EPR-entangled quantum frequency comb (QFC) under varying dispersion conditions.

2. Simulation Model of Microring Resonators

The pump light in the bus waveguide is coupled to the ring waveguide through resonant constructive interference, facilitating the spontaneous FWM process that generates a quantum optical frequency comb. This third-order nonlinear interaction, illustrated in **Figure 1**, follows the principles of energy conservation. The continuous-wave pump light (Ω_p) initiates FWM, resulting in the generation of signal (Ω_s) and idler (Ω_i) modes, which redistribute energy across different modes.

$$2\Omega_p = \Omega_s + \Omega_i \tag{1}$$

Momentum conservation is typically expressed by the following equation:

$$2\vec{k}_p - \vec{k}_s - \vec{k}_i = \vec{0} \tag{2}$$

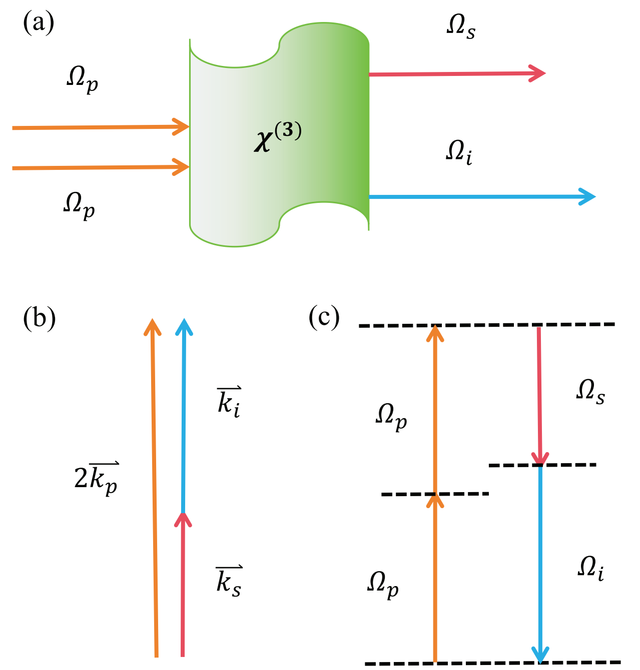

Figure 1. a) A schematic illustration of the third-order nonlinear process involved in generating Kerr optical frequency combs. b) Momentum conservation as it applies to the four-wave mixing process. c) Energy conservation in the context of four-wave mixing.

Figure 2a illustrates a typical microresonator configuration featuring an additional coupling structure, designed in accordance with OPO theory. The on-chip microring resonator is composed of a ring waveguide and a bus waveguide, with silicon nitride rib waveguides embedded in a silicon dioxide cladding. The coupling region and its corresponding input-output schematic are shown in Figure 2b. As shown in Figure 2a, the optical field propagates along the x-axis, and the effective cross-sectional area A_{eff} of the ring waveguide[36] is described by Equation (3). This area quantifies the extent to which the optical field is confined within the resonator. A smaller effective mode area indicates stronger confinement of the optical field by the resonator.

$$A_{\mathrm{eff}} = \frac{\left(\iint_{-\infty}^{+\infty} |F(y,z)|^2 \, dy \, dz \right)^2}{\iint_{-\infty}^{+\infty} |F(y,z)|^4 \, dy \, dz} \tag{3}$$

where $F(y,z)$ represents the modal distribution in silicon nitride and silicon dioxide, and we presume that this distribution remains time-invariant within the resonator.

The geometry of the coupling region directly affects the ring-bus coupling rate, facilitating the extraction of this rate and providing insight into the resonator's input-output characteristics.

In this analysis, we focus exclusively on the fundamental TE mode. The Lorentzian profile of the cavity resonance is depicted in **Figure 3** (shaded area). Figure 3b,c shows enlarged views under anomalous and normal dispersion conditions, respectively. The resonances shift across the spectrum due to the frequency dependence of the material's refractive index $n(\omega)$. To modify cavity parameters such as detuning, dispersion, coupling, temperature, and loss rate within our design platform, a solid theoretical foundation is required.

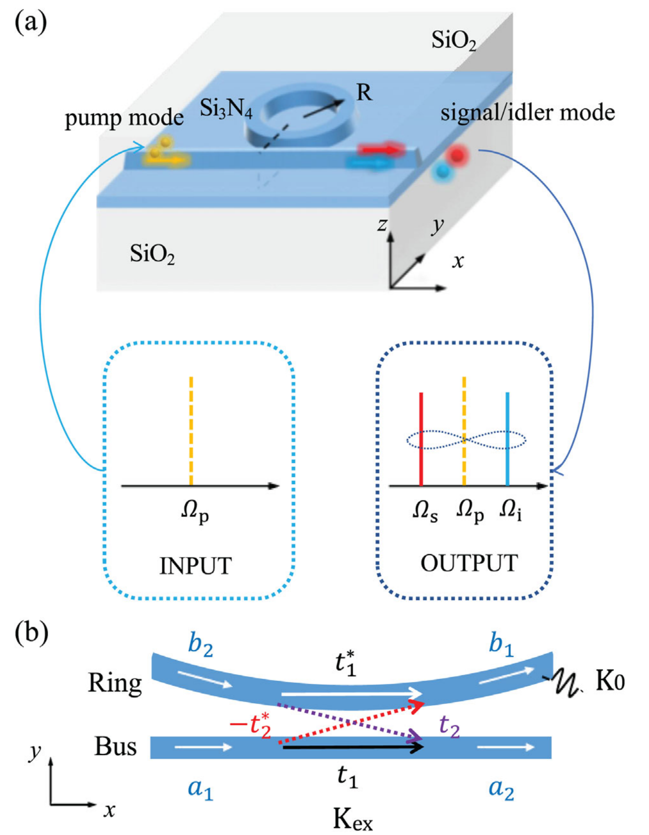

Figure 2. On-chip add-drop microring resonator. a) A 3D illustration of the resonator, with R representing the mean radius of the ring waveguide. b) A close-up of the coupling region along with the input-output schematic. Here, κ_0 denotes the intrinsic loss coupling rate, while κ_{ex} indicates the ring-to-bus coupling rate. The parameters t_1 and t_2 are related by $|t_1|^2 + |t_2|^2 = 1$. Note that the bus waveguides do not have to be straight.

2.1. Detuning, Dispersion and Temperature

This subsection delves into the intricacies of detuning and dispersion. We introduce the relative mode number l ($l \in \mathbb{Z}$) to identify modes close to the pump mode ω_0 ($l = 0$). A Taylor expansion is applied to the resonant modes in the vicinity of ω_0:

$$\omega_l = \omega_0 + D_1 l + \frac{D_2}{2} l^2 + \cdots = \omega_0 + \sum_{\mathrm{n}=1}^{\infty} D_{\mathrm{n}} \frac{l^{\mathrm{n}}}{\mathrm{n}!} \tag{4}$$

Here, we define $D_1 = 2\pi v_f$, where v_f represents the free spectral range (FSR). The parameter D_2 governs group velocity dispersion,[37] with $D_2 > 0$ corresponding to anomalous dispersion and $D_2 < 0$ indicating normal dispersion. Higher-order dispersion terms are disregarded, i.e., $D_n = 0$ for $n \geq 3$. The integrated dispersion is given by: $D_{\mathrm{int}} = \omega_l - \omega_0 - D_1 l$,[38] which is well approximated by a quadratic polynomial around ω_0. A comparative analysis of anomalous and normal dispersion is performed for silicon nitride microring resonators.

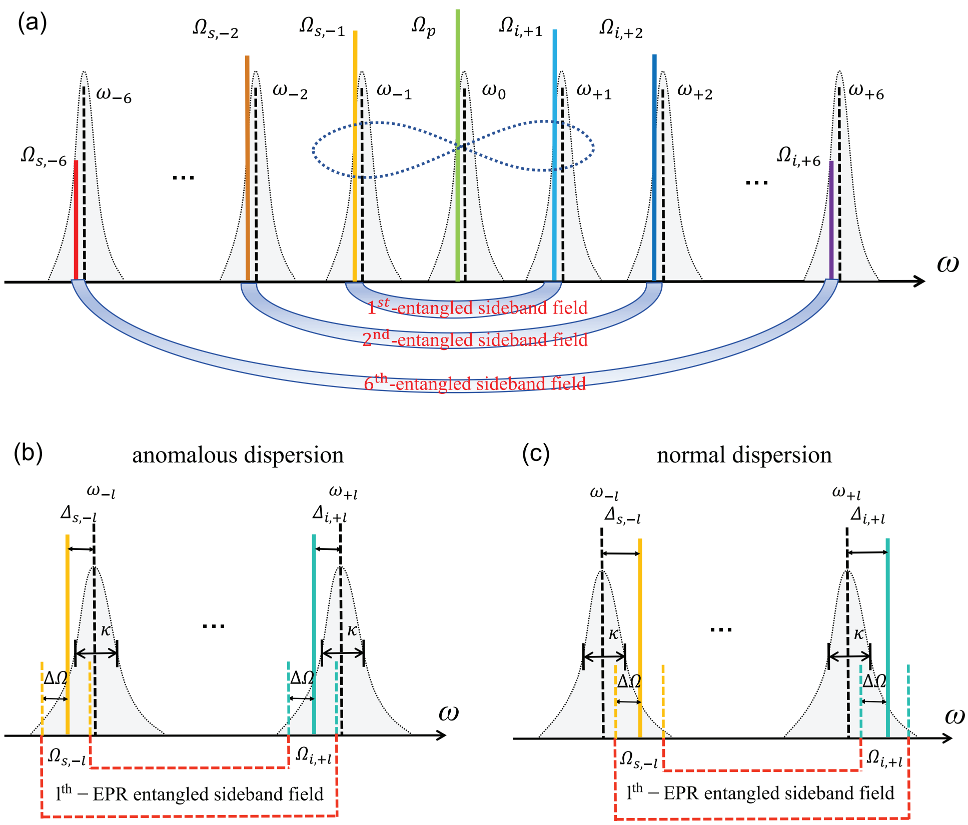

Figure 3. a) Resonances with anomalous dispersion. The solid lines indicate the evenly spaced positions of the output comb lines, while the gray slashes mark the positions of the resonances under anomalous dispersion. b) An enlarged subgraph. For mode 0, the relationship between the laser frequency Ω_0 (or Ω_p), cold-resonance frequency ω_0, loaded linewidth κ, and the normalized cold cavity pump detuning is expressed as $\sigma_c = \omega_0 - \Omega_0$. For mode $+l$, the normalized cold cavity detuning is $\Delta_{i,+l} = \omega_{+l} - \Omega_{i,+l}$, with the assumption that all modes share the same linewidth κ. c) Enlarged view for the case of normal dispersion.

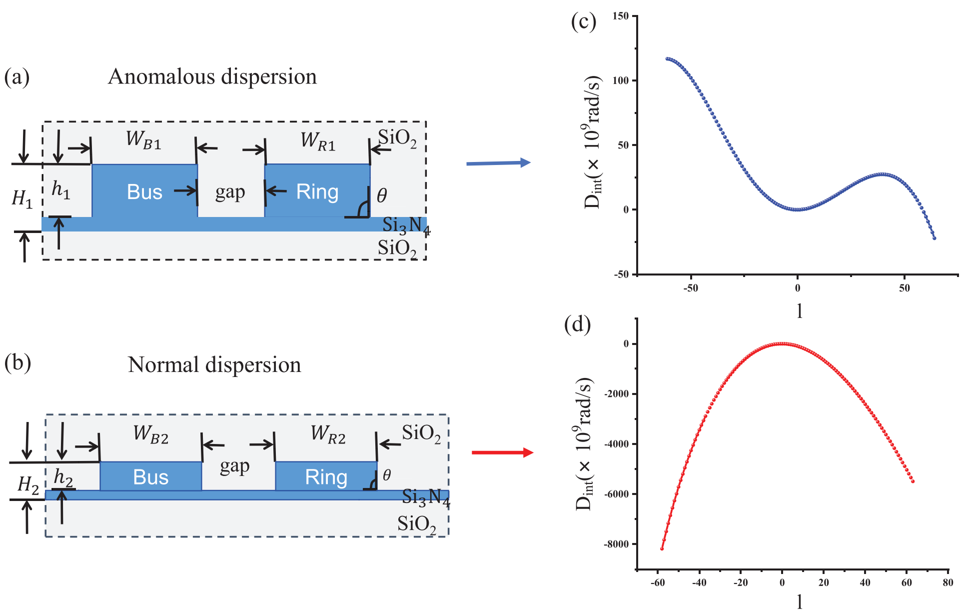

Figure 4. a) Profile of rib waveguides under anomalous dispersion. b) Profile of rib waveguides under normal dispersion. c) Dispersion simulation curve under anomalous dispersion.Here, l represents the relative mode number. d) Dispersion simulation curve under normal dispersion.

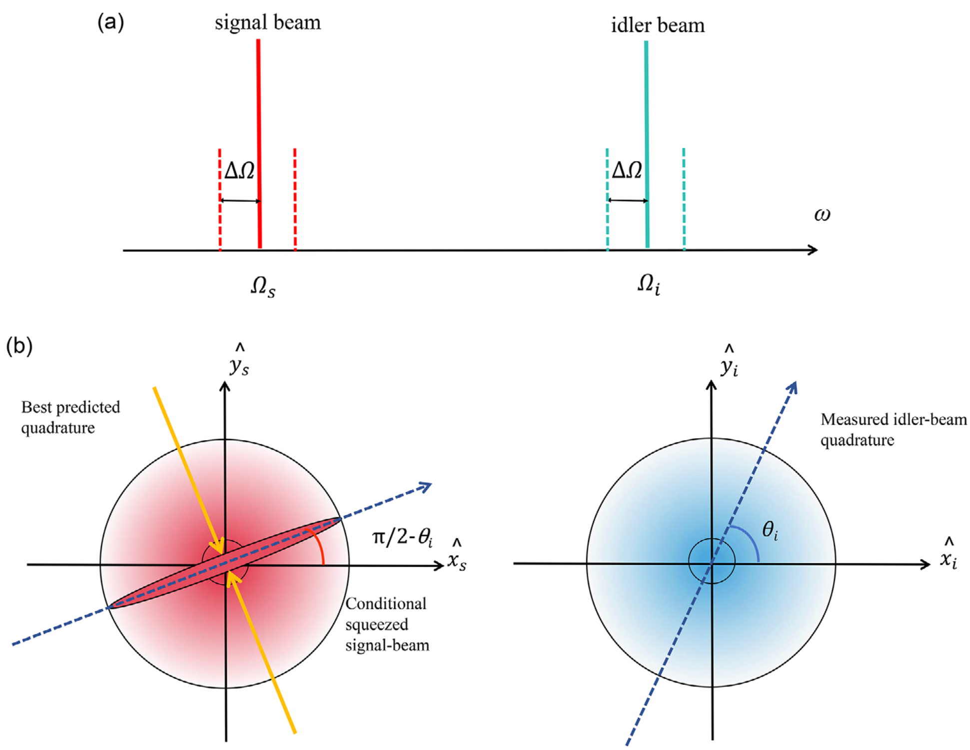

Figure 5. a) The spectral decomposition of EPR-entangled beams, as referenced in Figure 3. b) Quantum statistics of the signal and idler beams.

In this investigation, we presume a homogeneous temperature distribution throughout the microring resonator at any given instant. The temperature-induced shift in resonance frequencies at a temperature T is expressed as:

$$\omega_l(T) = \omega_l(T_0)\left[1 - \left(\frac{\alpha_n}{n_{eff}} + \alpha_L\right)\Delta T\right] \tag{5}$$

where $\Delta T = T - T_0$ denotes the deviation from the reference temperature $T_0 = 20\ ^\circ\mathrm{C}$. The thermo-optic coefficient α_n and the thermal expansion coefficient α_L for Si_3N_4 are $2.45 \times 10^{-5}\ /^\circ\mathrm{C}$ and $3.30 \times 10^{-6}\ /^\circ\mathrm{C}$, respectively.[39,40] At the frequency ω_0, the effective refractive index is $n_{eff} = 1.836$ under anomalous dispersion, while it is $n_{eff} = 1.702$ under normal dispersion.

For simplification, we neglect the pump power, assuming its contribution to the frequency shift induced by nonlinear effects is negligible. Consequently, only the thermally induced shift in resonance frequencies is considered. The detuning of the pump frequency at temperature T is given by:

$$\sigma_c = \omega_0(T) - \Omega_0(T) \tag{6}$$

The comb lines of QFCs remain evenly spaced, independent of temperature, and are unaffected by D_{int}:

$$\Omega_l(T) = \Omega_0(T) + D_1 l \tag{7}$$

At the reference temperature T_0, the resonance frequencies are expressed as:

$$\omega_l(T_0) = \omega_0(T_0) + D_1 l + D_2 \frac{l^2}{2} \tag{8}$$

From Equations (5)– (8), the normalized cold cavity detuning $\Delta_{c,l}$ for mode l is:

$$\Delta_{c,l} = \omega_l(T) - \Omega_l(T) = \sigma_c + \frac{D_2}{2} l^2 - \delta_T \tag{9}$$

where $\delta_T = \left(D_1 l + \frac{D_2}{2} l^2\right)\left(\frac{\alpha_n}{n_0} + \alpha_L\right)\Delta T$. This equation establishes the relationship between detuning, dispersion, and intracavity temperature.

2.2. Coupling, Loss, and Gap

This section delves into the intricate relationship between input-output parameters, such as the coupling rate (γ) and loss rate (μ), and the fundamental intrinsic cavity properties, including the coupling coefficient (κ) and the quality factor. The resonator loss is conceptualized as an effective phantom channel, as outlined in refs. [41, 42], leveraging the transmission characteristics of a beam splitter to ensure that the coupling and loss rates fulfill the requisite conditions $\gamma \ll \nu_f$ and $\mu \ll \nu_f$, where ν_f denotes the free spectral range. As depicted in Figure 2b, the coupling rate is represented as: $\gamma = |t_2|^2 \nu_f = (1 - |t_1|^2)\nu_f$, and the loss rate simplifies to: $\mu = \alpha_L \nu_f$, where $L = 2\pi R$ is the circumference of the microring resonator, and $R = \frac{D_{\mathrm{in}} + D_{\mathrm{out}}}{4}$ is the radius, with D_{in} and D_{out}

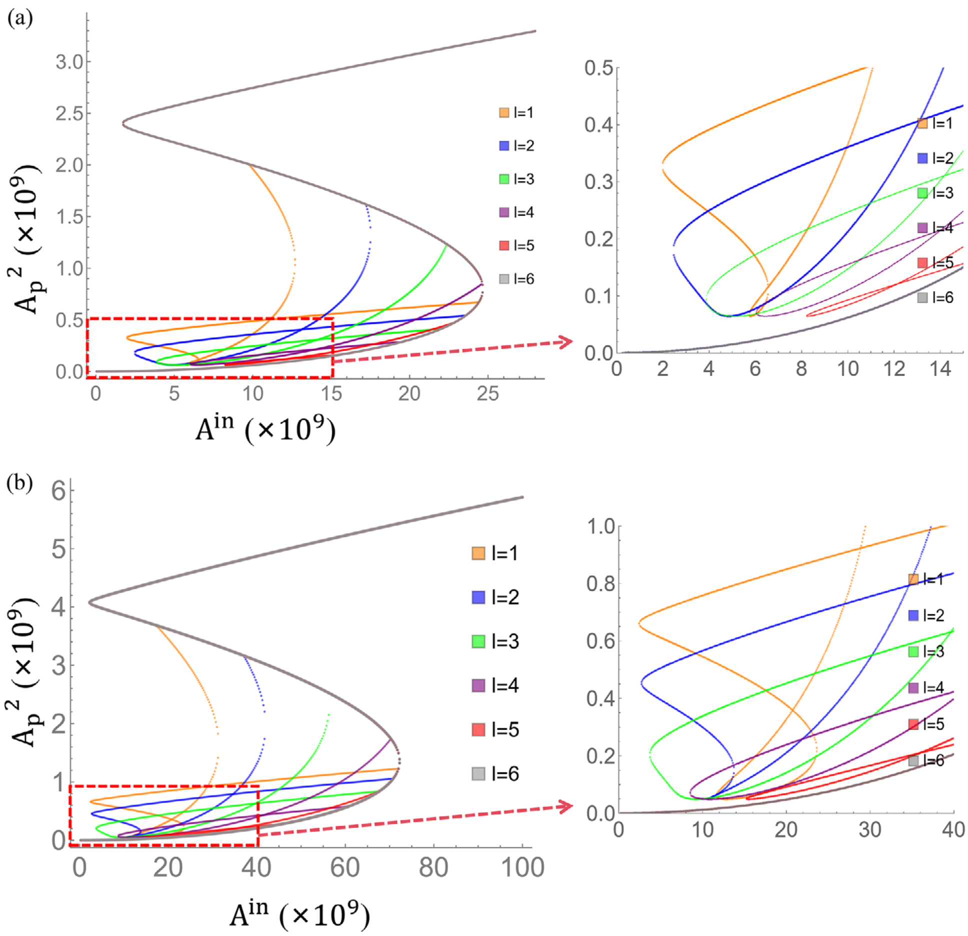

Figure 6. The variation of the intracavity pump mode amplitude with respect to the injected pump amplitude in our QFC. a) Under anomalous dispersion($\sigma_c = 8$ GHz). b) Under normal dispersion ($\sigma_c = 18$ GHz).

representing the inner and outer diameters of the microring, respectively. Furthermore, the absorption coefficient α, expressed in units of m^{-1}, is approximately given by: $\alpha \approx \frac{f_0}{Q_0 \cdot R \cdot v_f}$, where f_0 (Hz) denotes the resonance frequency.

Next, we set $b_2 = 0$ and systematically vary the gap, defined as the distance between the ring waveguide and the bus waveguide, to scan the transmission from the added port to the through port ($|t_1|^2$). The ratio $r = \frac{\gamma}{\mu}$ quantifies the relationship between the coupling rate (γ) and the internal loss rate (μ). When $r < 1$, this signifies under-coupling; $r > 1$ corresponds to over-coupling; and $r = 1$ represents the condition of critical coupling. In our simulation, we prioritize over-coupled configurations, which, although leading to a reduction in intracavity power, facilitating more efficient power extraction from the resonator.

For resonators employed in the generation of quantum optical frequency combs, the quality factor Q is a pivotal parameter. The Q-factor governs the resonator's ability to achieve substantial field enhancement and reflects the microcavity's efficiency in storing optical energy. It is mathematically expressed as:

$$Q = \omega_0 \tau_p = \frac{\omega_0}{\kappa} \tag{10}$$

Here, ω_0 represents the central frequency of the resonance peak, τ_p denotes the photon lifetime, and κ is the full width at half maximum of the resonance peak.[43] The loss coupling rate, κ_0 (in rad/s), is given by

$$\kappa_0 = \frac{\omega_0}{Q_0} \approx \frac{c\alpha_n}{n_g} = \mu \tag{11}$$

where n_g is the group refractive index of silicon nitride near Ω_0. The total loss rate is expressed as

$$\kappa = \kappa_0(1 + r) = \Gamma \tag{12}$$

and the ring-bus coupling rate κ_{ex} is given by

$$\kappa_{ex} = \kappa - \kappa_0 = \frac{\omega_0}{Q_{ex}} = \gamma \tag{13}$$

where Q_{ex} denotes the external quality factor.[44] The total quality factor Q satisfies the following relationship:

$$\frac{1}{Q} = \frac{1}{Q_0} + \frac{1}{Q_{ex}} \tag{14}$$

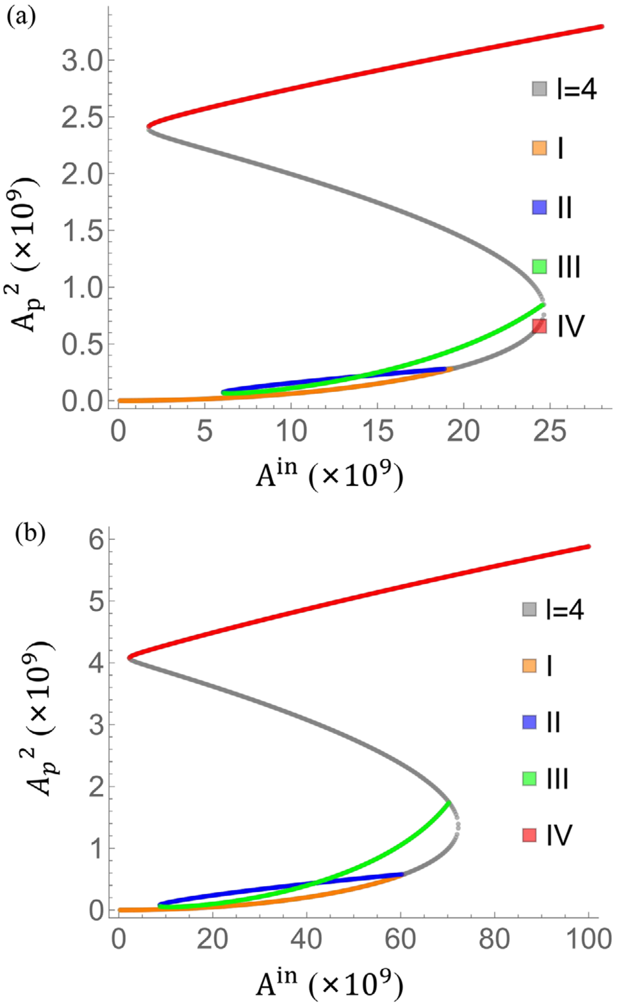

Figure 7. The variation of the intracavity pump mode amplitude with respect to the injected pump amplitude for the fourth mode. a) Under anomalous dispersion(σ_c = 8 GHz). b) Under normal dispersion (σ_c = 18 GHz).

Thus, the gap can be directly linked to Q_{ex} via the coupling ratio r.

2.3. Actual Simulation

Our objective is to design a dispersion-flattened waveguide to mitigate phase mismatch in the FWM process. By tuning the parameters of the silicon nitride integrated microcavity structure–such as its geometry, size, and the selection of nonlinear materials–the dispersion characteristics can be adjusted to achieve phase matching. Dispersion engineering is essential for generating a larger number of operationally entangled state pairs. Optimal phase matching conditions are ensured by fine-tuning D_{int} to approach zero over the broadest possible spectral range.

$$\Delta k = \frac{2\omega_p n(\omega_p)}{c} - \frac{\omega_s n(\omega_s)}{c} - \frac{\omega_i n(\omega_i)}{c} \quad (15)$$

We utilize COMSOL Multiphysics to model the waveguide's overall geometry and the integrated dispersion profile. A fifth-order polynomial fitting procedure is employed to extract parameters that exhibit a close alignment with the integrated dispersion D_{int}, as illustrated in **Figure 4**. In addition, Lumerical FDTD simulations are conducted to investigate the relationship between the gap and the coupling coefficient. Assuming an intrinsic quality factor of $Q_0 = 10^6$, we compute $\kappa_0 = 1.21 \times 10^9$. With a coupling ratio $r = \frac{\gamma}{\mu} = 1.222$, which corresponds to an over-coupled regime, the external quality factor is subsequently determined as $Q_{\mathrm{ex}} = Q_0/r = 8.18 \times 10^5$. The gap is calculated to be 490 nm based on the results from Lumerical FDTD simulations.

For both anomalous and normal dispersion regimes, we design two distinct microcavity structures, each capable of generating classical optical solitons. The waveguide geometry is meticulously selected to ensure optimal dispersion characteristics for the specified regime, facilitating the generation of multiple EPR entangled pairs. Figure 4a illustrates the micro-ring structure under anomalous dispersion conditions, with a radius of $R = 23\,\mu$m, waveguide and bus widths of $W_{R1} = W_{B1} = 1610$ nm, heights of $H_1 = h_1 = 800$ nm, and an angle of $\theta = 90°$. Simulation results for this configuration yield a free spectral range ν_f of 989.592 GHz, a mode 0 frequency f_0 of 193.251 THz, a second-order dispersion coefficient D_2 of $1.435 \times 2\pi \times 10^7$ rad s^{-1}, and an effective area A_{eff} of 1.10 μm^2. Figure 4b depicts the micro-ring structure under normal dispersion conditions, with parameters: radius $R = 23\,\mu$m, waveguide and bus widths of $W_{R2} = W_{B2} = 1710$ nm, heights of $H_2 = h_2 = 400$ nm, and the same angle $\theta = 90°$. For this configuration, the simulation results show a free spectral range ν_f of 1019.553 GHz, a mode 0 frequency f_0 of 193.797 THz, a second-order dispersion coefficient D_2 of $-5.676 \times 2\pi \times 10^8$ rad s^{-1}, and an effective area A_{eff} of 0.968 μm^2.

3. EPR Entanglement Dynamics

In this section, the quantum dynamics of the resonator are elucidated, building upon the theoretical framework delineated in Section 2.

3.1. Hamiltonian

The system Hamiltonian encapsulates the optical nonlinear dynamics within the quantum regime, with each resonant mode represented by an annihilation operator $\hat{a}_j$, where $j = p, s, i$. In the context of FWM, the system's total energy is partitioned into the free Hamiltonian $\hat{H}_0$ and the nonlinear Hamiltonian $\hat{H}_{NL}$, as:

$$\hat{H} = \hat{H}_0 + \hat{H}_{NL} \quad (16)$$

The free Hamiltonian $\hat{H}_0$ is expressed as:

$$\hat{H}_0 = \hbar\left(\omega_p \hat{a}_p^\dagger \hat{a}_p + \omega_s \hat{a}_s^\dagger \hat{a}_s + \omega_i \hat{a}_i^\dagger \hat{a}_i\right) \quad (17)$$

For the FWM process, the nonlinear Hamiltonian[45,46] is generally decomposed as:

$$\hat{H}_{\mathrm{NL}} = \hat{H}_{\mathrm{SPM}} + \hat{H}_{\mathrm{XPM}} + \hat{H}_{\mathrm{FWM}} \quad (18)$$

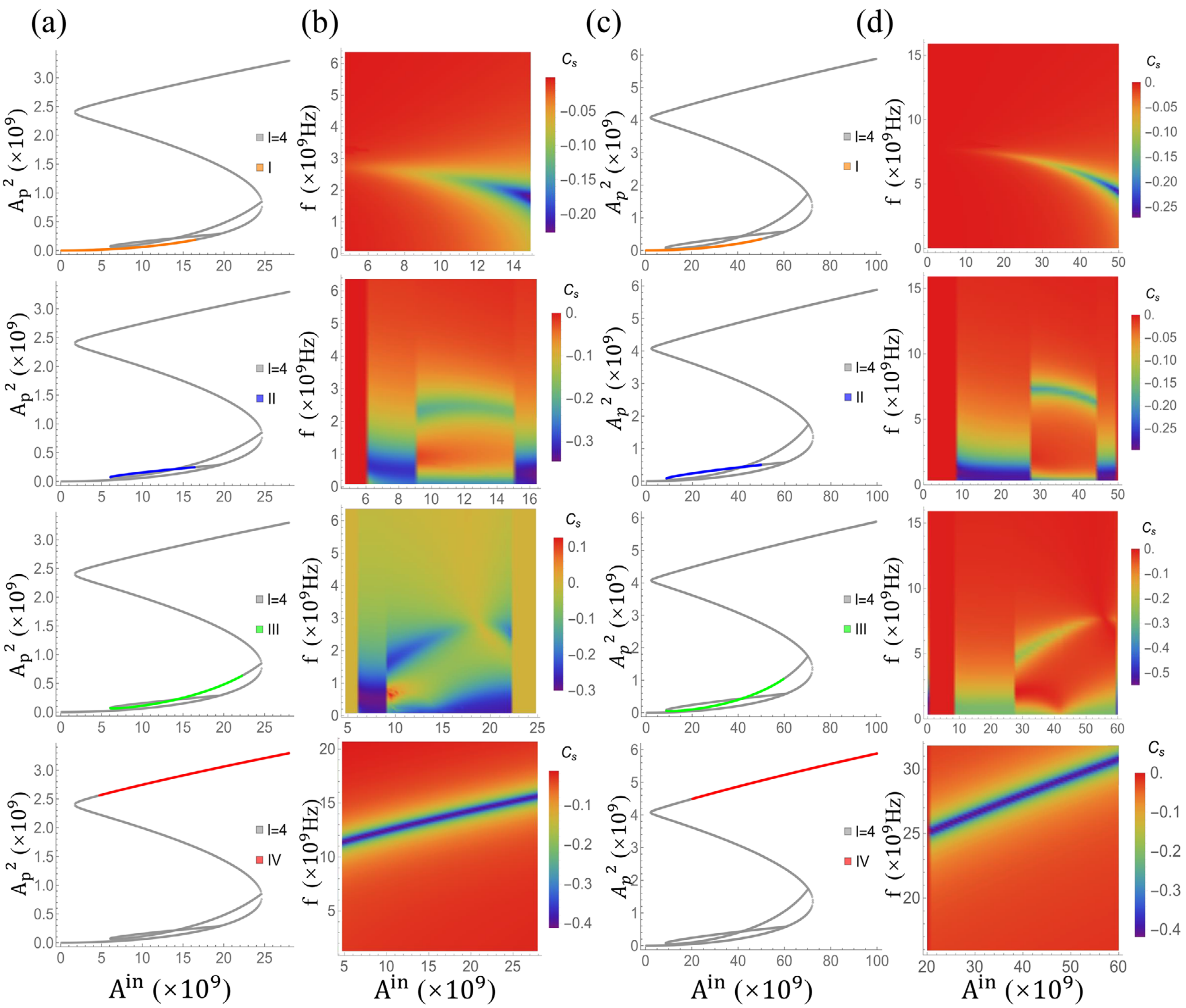

Figure 8. a) The four distinct stages of the fourth mode under anomalous dispersion. b) Entanglement distribution in the $A^{in} - f$ plane under anomalous dispersion (σ_c = 8 GHz, r = 1.222). c) The four stages of the fourth mode under normal dispersion. d) Entanglement distribution in the $A^{in} - f$ plane under normal dispersion (σ_c = 18 GHz, r = 1.222).

The terms $\hat{H}_{SPM}$, $\hat{H}_{XPM}$, and $\hat{H}_{FWM}$ correspond to the self-phase modulation (SPM), cross-phase modulation (XPM), and FWM processes, respectively. These nonlinear phenomena fundamentally govern the oscillatory dynamics, noise characteristics, and entanglement properties of the system. Among these effects, FWM plays a pivotal role in facilitating energy exchange between the resonant modes. The nonlinear Hamiltonian $\hat{H}_{NL}$ is formulated as:

$$\begin{aligned}\hat{H}_{\mathrm{NL}} = -\hbar\eta\Big[&\frac{1}{2}\left(\hat{a}_p^\dagger\hat{a}_p^\dagger\hat{a}_p\hat{a}_p + \hat{a}_s^\dagger\hat{a}_s^\dagger\hat{a}_s\hat{a}_s + \hat{a}_i^\dagger\hat{a}_i^\dagger\hat{a}_i\hat{a}_i\right)\\ &+ 2\left(\hat{a}_p^\dagger\hat{a}_s^\dagger\hat{a}_p\hat{a}_s + \hat{a}_p^\dagger\hat{a}_i^\dagger\hat{a}_p\hat{a}_i + \hat{a}_s^\dagger\hat{a}_i^\dagger\hat{a}_s\hat{a}_i\right)\\ &+\left(\hat{a}_s^\dagger\hat{a}_i^\dagger\hat{a}_p\hat{a}_p + \hat{a}_p^\dagger\hat{a}_p^\dagger\hat{a}_s\hat{a}_i\right)\Big]\end{aligned} \tag{19}$$

The nonlinear coupling coefficient η is bounded from below as: $\eta = \hbar\omega_0^2 c n_2/(n_0^2 V_{\mathrm{eff}})$. This parameter quantifies the frequency shift per photon induced by the $\chi^{(3)}$ nonlinearity.[47] Here, c denotes the speed of light in a vacuum, and n_2, the nonlinear refractive index of Si_3N_4, is intrinsically correlated with the material's linear refractive index, n_0. In our Si_3N_4 microresonator, n_2 is specified as 2.6×10^{-19} m^{2}W^{-1}. The effective mode volume V_{eff} is rigorously defined through the integral form:

$$V_{\mathrm{eff}} = \frac{\int n_0^2|F(x,y,z)|^2 dV \int |F(x,y,z)|^2 dV}{\int n_0^2 |F(x,y,z)|^4 dV} \tag{20}$$

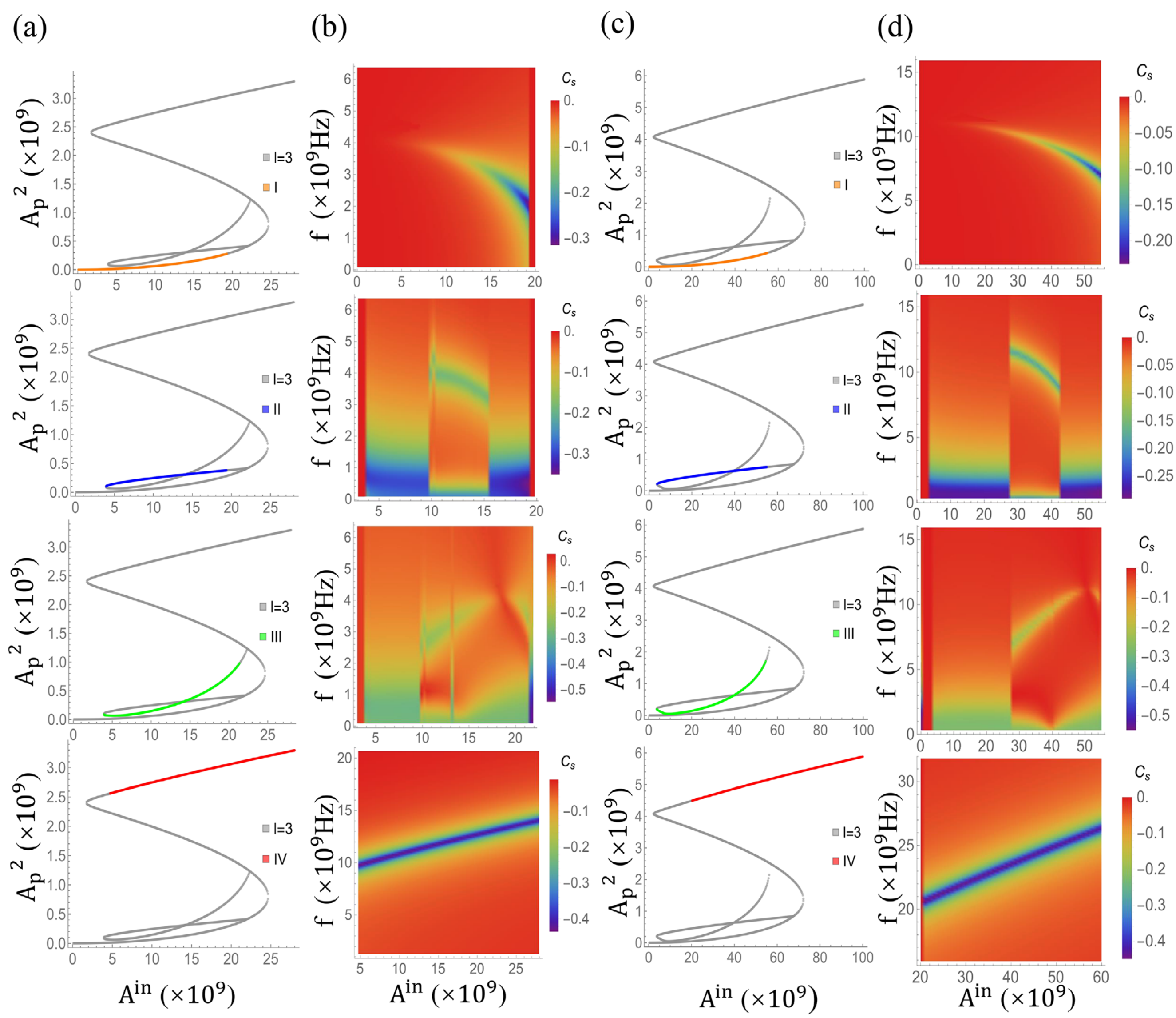

Figure 9. a) The four distinct stages of the third mode under anomalous dispersion. b) Entanglement distribution in the $A^{in} - f$ plane under anomalous dispersion ($\sigma_c = 8$ GHz, $r = 1.222$). c) The four stages of the fourth mode under normal dispersion. d) Entanglement distribution in the $A^{in} - f$ plane under normal dispersion ($\sigma_c = 18$ GHz, $r = 1.222$).

For a microring resonator operating in whispering-gallery-mode (WGM), an approximate upper bound for V_{eff} can be formulated as $V_{\text{eff}} \approx A_{\text{eff}} \cdot 2\pi R$.

3.2. Heisenberg–Langevin Equations

The Heisenberg–Langevin equations[48] integrate the Heisenberg equations of motion with Langevin noise terms to capture the dynamics of open quantum systems under the influence of quantum noise. The resulting formalism is expressed as:

$$\frac{d\hat{a}_j}{dt} = -\frac{i}{\hbar}[\hat{a}_j, \hat{H}] - \kappa \sum_j \hat{a}_j + \sqrt{2\kappa_{ex}} \sum_j \hat{a}_j^{\text{in}} + \sqrt{2\kappa_0} \sum_j \hat{a}_j^{\text{loss}}, \quad j = p, s, i. \tag{21}$$

Here, the modes under consideration are presumed to exhibit analogous field profiles, characterized by a unified total loss rate κ, which comprises the intrinsic loss rate κ_0 and the coupling rate between the ring and bus waveguides, κ_{ex}, satisfying $\kappa = \kappa_0 + \kappa_{\text{ex}}$. The annihilation operators $\hat{a}_{\text{in}}$ and $\hat{a}_{\text{loss}}$ represent the resonator's input and loss modes, respectively. In this framework, the loss modes are assumed to be in vacuum states, with the incident signal and idler modes similarly treated as vacuum states. The expectation value of the input pump mode is expressed as:

$$\left\langle \hat{a}_p^{\text{in}}(t) \right\rangle = A^{\text{in}} = \sqrt{\frac{P_{\text{in}}}{\hbar\Omega_0}} \tag{22}$$

where P_{in} (Watt) is the pump laser power in the bus waveguide.

By applying the rotating wave approximation (RWA), where $\hat{a}^j e^{-i\omega_j t}$ substitutes $\hat{a}^j$, the Heisenberg–Langevin equations governing the dynamics of the pump, signal, and idler modes are formulated as:

$$\begin{cases} \frac{d\hat{a}_p}{dt} = i\eta\left(\hat{a}_p^\dagger\hat{a}_p\hat{a}_p + 2\hat{a}_s^\dagger\hat{a}_s\hat{a}_p + 2\hat{a}_i^\dagger\hat{a}_i\hat{a}_p + 2\hat{a}_p^\dagger\hat{a}_s\hat{a}_i\right) \\ \qquad - \kappa\hat{a}_p - i\sigma_c\hat{a}_p + \sqrt{2\kappa_{ex}}\hat{a}_p^{in} + \sqrt{2\kappa_0}\hat{a}_p^{loss} \\ \frac{d\hat{a}_s}{dt} = i\eta\left(2\hat{a}_p^\dagger\hat{a}_p\hat{a}_s + \hat{a}_s^\dagger\hat{a}_s\hat{a}_s + 2\hat{a}_i^\dagger\hat{a}_i\hat{a}_s + \hat{a}_p^2\hat{a}_i^\dagger\right) \\ \qquad - \kappa\hat{a}_s - i\Delta_{-l}\hat{a}_s + \sqrt{2\kappa_{ex}}\hat{a}_s^{in} + \sqrt{2\kappa_0}\hat{a}_s^{loss} \\ \frac{d\hat{a}_i}{dt} = i\eta\left(2\hat{a}_p^\dagger\hat{a}_p\hat{a}_i + 2\hat{a}_s^\dagger\hat{a}_s\hat{a}_i + \hat{a}_i^\dagger\hat{a}_i\hat{a}_i + \hat{a}_p^2\hat{a}_s^\dagger\right) \\ \qquad - \kappa\hat{a}_i - i\Delta_{+l}\hat{a}_i + \sqrt{2\kappa_{ex}}\hat{a}_i^{in} + \sqrt{2\kappa_0}\hat{a}_i^{loss} \end{cases} \tag{23}$$

where Δ_{-l} and Δ_{+l} denote the normalized cold cavity detunings associated with the signal and idler modes, respectively. Notably, κ_{ex} and κ_0 remain constant, independent of the mode number l.

3.3. Steady-State Equations

We employ a linearization technique by representing each field operator $\hat{a}_j$ as the sum of its steady-state mean value α_j and a fluctuation term $\delta\hat{a}_j$, such that $\hat{a}_j = \alpha_j + \delta\hat{a}_j$. In the steady-state regime, α_j assumes a constant value, allowing us to set $\delta\hat{a}_j = 0$ and $\frac{d\alpha_j}{dt} = 0$, thereby yielding the steady-state Heisenberg–Langevin equations. Under these assumptions, the input fields for the signal and idler modes, as well as the loss modes for the pump, signal, and idler, are considered to be in a vacuum state, resulting in $\alpha_s^{in} = \alpha_i^{in} = \alpha_j^{loss} = 0$.

Without restricting the generality, we adopt the phase of the external pump as the reference. This leads to the following definitions: $\alpha_j = A_j e^{i\theta_j}$, $\alpha_p^{in} = A^{in}e^{i\theta_{in}}$, $\Theta = \theta_s + \theta_i - 2\theta_p$, $\psi = \theta_{in} - \theta_p$. For the sake of simplicity, we set $A_s = A_i = A$ and $\Delta_{+l} = \Delta_{-l} = \Delta$. The external pump power is defined as $F = \sqrt{\frac{2\gamma\eta}{\hbar\Omega_0\Gamma^3}P_{in}}$,[49] with $A^{in} = F\sqrt{\frac{\Gamma^3}{2\gamma\eta}}$. Leveraging these parameters, we derive the subsequent expressions:

$$\begin{cases} A_p^4 &= 1 + \left(\sigma_c - \frac{D_3}{2} - 2A_p^2 - 3A^2\right)^2 \\ F^2 &= A_p^2\left(1 + 2\frac{A^2}{A_p^2}\right)^2 \\ & \quad + A_p^2[\sigma_c - A_p^2 - 2\frac{A^2}{A_p^2}\left(\sigma_c - \frac{D_3}{2} - 3A^2\right)]^2 \\ \sin(\Theta) &= \frac{1}{A_p^2} \\ \cos(\Theta) &= \frac{1}{A_p^2}\left(\Delta - 3A^2 - 2A_p^2\right) \\ \sin(\psi) &= \frac{A_p}{F}\left[\sigma_c - A_p^2 - 2\frac{A^2}{A_p^2}\left(-3A^2 - \frac{D_3}{2} + \sigma_c\right)\right] \\ \cos(\psi) &= \frac{A_p}{F}\left(1 + 2\frac{A^2}{A_p^2}\right) \end{cases} \tag{24}$$

Equation (24) encompasses several critical variables: A_p, A^{in}, A, σ_c, and Δ. By assigning specific numerical values to any two of these parameters, a numerical relationship can be derived for the remaining three. Consequently, two of the remaining variables can be expressed as functions of the third.

3.4. Quantum Fluctuations

To scrutinize the quantum characteristics of the signal and idler modes, we derive the quantum fluctuation equations from Equation (23). Since the steady-state solutions have been meticulously established, the fluctuation equations are extracted by subtracting the steady-state components from Equation (23). In this analysis, the pump field is treated as a classical parameter, thereby disregarding fluctuations in the pump mode ($\delta\hat{a}_p = 0$), with higher-order fluctuation terms omitted for conciseness.

We introduce a fluctuation vector for the signal and idler modes as follows:

$$\delta\hat{\mathbf{A}} = \left(\delta\hat{a}_s e^{-i\theta_s}, \delta\hat{a}_s^\dagger e^{i\theta_s}, \delta\hat{a}_i e^{-i\theta_i}, \delta\hat{a}_i^\dagger e^{i\theta_i}\right)^T \tag{25}$$

where θ_j denotes the phase of the steady-state mean value $\alpha_j = A_j e^{i\theta_j}$. The temporal evolution of the fluctuations $\delta\hat{a}_j$ is governed by the following set of linearized equations:

$$\frac{d\delta\hat{\mathbf{A}}}{dt} = M_a \cdot \delta\hat{\mathbf{A}} + T_a^{in} \cdot \delta\hat{\mathbf{A}}^{in} + T_a^{loss} \cdot \delta\hat{\mathbf{A}}^{loss} \tag{26}$$

where $T_a^{in} = \text{diag}\left(\sqrt{2\kappa_{ex}}, \sqrt{2\kappa_{ex}}, \sqrt{2\kappa_{ex}}, \sqrt{2\kappa_{ex}}\right)$, $T_a^{loss} = \text{diag}\left(\sqrt{2\kappa_0}, \sqrt{2\kappa_0}, \sqrt{2\kappa_0}, \sqrt{2\kappa_0}\right)$. The matrix M_a originates from the linearization procedure, with its components determined by the mean field values and the detuning parameters.

The frequency-domain evolution of these fluctuations can be captured through a Fourier transform. This transformation, combined with the resonator's input-output relations $\hat{a}^{out} = -\hat{a}^{in} + \sqrt{2\kappa_{ex}}\hat{a}$, offers a comprehensive description of the system's behavior:

$$\begin{aligned} \delta\hat{\mathbf{A}}^{out}(\omega) &= -\delta\hat{\mathbf{A}}^{in} + T_a\delta\hat{\mathbf{A}} \\ &= [T_a\left(i\omega I - M_a\right)^{-1}T_a^{in} - I] \cdot \delta\hat{\mathbf{A}}^{in} \\ &+ T_a\left(i\omega I - M_a\right)^{-1}T_a^{loss} \cdot \delta\hat{\mathbf{A}}^{loss} \end{aligned} \tag{27}$$

where $T_a = \text{diag}\left(\sqrt{2\kappa_{ex}}, \sqrt{2\kappa_{ex}}, \sqrt{2\kappa_{ex}}, \sqrt{2\kappa_{ex}}\right)$, and I is the identity matrix.

Thus, the output spectral noise density matrix can be expressed as:

$$\begin{aligned} S_a(\omega) &= \left\langle \delta\hat{\mathbf{A}}^{out}(\omega)\delta\hat{\mathbf{A}}^{out,T}(-\omega)\right\rangle \\ &= [T_a\left(i\omega I - M_a\right)^{-1}T_a^{in} - I] \cdot M_c \\ &\cdot [T_a\left(-i\omega I - M_a\right)^{-1}T_a^{in} - I]^T + T_a\left(i\omega I - M_a\right)^{-1} \\ &\cdot T_a^{loss} \cdot M_c \cdot [T_a\left(-i\omega I - M_a\right)^{-1}T_a^{loss}]^T \end{aligned} \tag{28}$$

where the matrix $M_c = \begin{pmatrix} 0 & 1 & 0 & 0 \\ 0 & 0 & 0 & 0 \\ 0 & 0 & 0 & 1 \\ 0 & 0 & 0 & 0 \end{pmatrix}$.

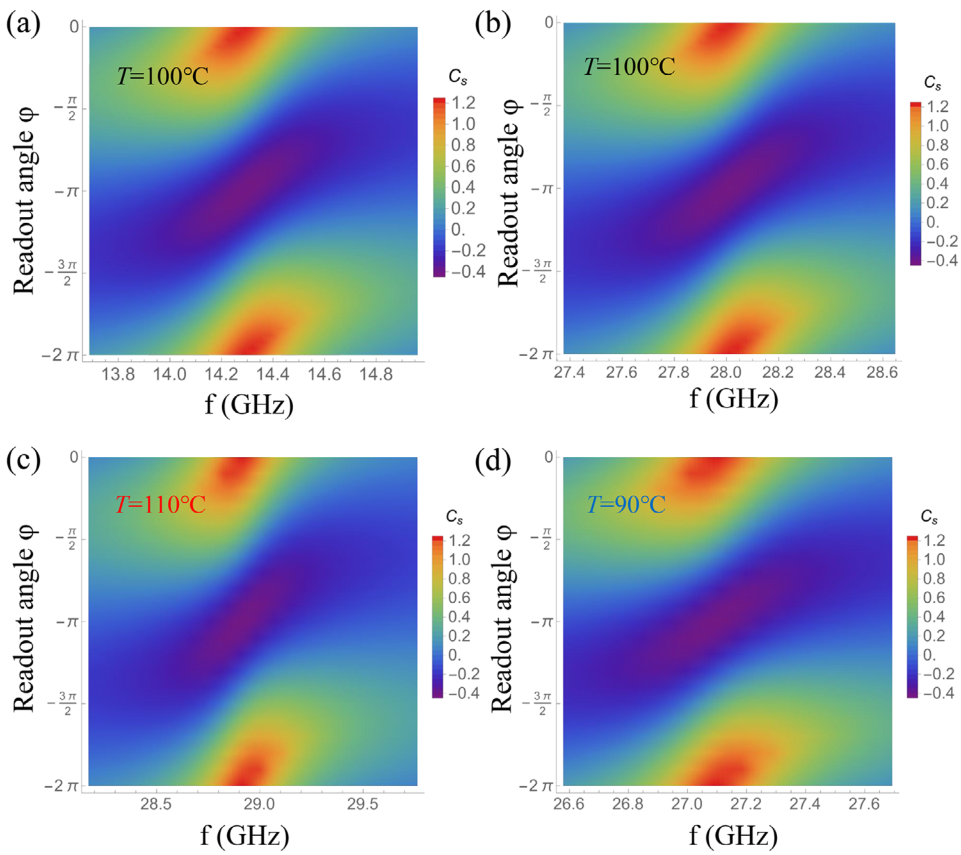

Figure 10. The relationship diagram between the entanglement degree C_s, the observation frequency f (where $f = \frac{\Delta\Omega}{2\pi}$), and the readout angle, showing frequency-dependent squeezing via Einstein–Podolsky–Rosen entanglement. a) Under anomalous dispersion (σ_c = 8 GHz, r = 1.222, A^{in} = 1×10^{10} Vm^{-1}, T = 100 °C). b) Under normal dispersion (σ_c = 18 GHz, r = 1.222, A^{in} = 4×10^{10} Vm^{-1}, T = 100 °C). c) Under normal dispersion (σ_c = 18 GHz, r = 1.222, A^{in} = 4×10^{10} Vm^{-1}, T = 110 °C). d) Under normal dispersion (σ_c = 18 GHz, r = 1.222, A^{in} = 4×10^{10} Vm^{-1}, T = 90 °C).

3.5. EPR Entanglement and Criteria

To quantitatively assess the entanglement between the signal and idler modes, we employ the criterion from ref. [50] to compute the entanglement degree C_s. The amplitude $\hat{x}_j$ and phase $\hat{y}_j$ quadrature operators for each mode $j = s, i$ are defined as functions of the annihilation and creation operators $\hat{a}_j$ and $\hat{a}_j^\dagger$:[51]

$$\hat{x}_j = \frac{\hat{a}_j^\dagger + \hat{a}_j}{\sqrt{2}}, \quad \hat{y}_j = \frac{i\hat{a}_j^\dagger - i\hat{a}_j}{\sqrt{2}} \tag{29}$$

By rotating the detection angles of the signal and idler beams (θ_s, θ_i), we can obtain:

$$\left(\delta\hat{x}_s, \delta\hat{x}_i, \delta\hat{y}_s, \delta\hat{y}_i\right)^{\mathrm{T}} = P\left(\delta\hat{a}_s, \delta\hat{a}_s^\dagger, \delta\hat{a}_i, \delta\hat{a}_i^\dagger\right)^{\mathrm{T}} \tag{30}$$

where $\mathrm{P} = \frac{1}{\sqrt{2}}\begin{pmatrix} e^{-i\theta_s} & e^{i\theta_s} & 0 & 0 \\ 0 & 0 & e^{-i\theta_i} & e^{i\theta_i} \\ -ie^{-i\theta_s} & ie^{i\theta_s} & 0 & 0 \\ 0 & 0 & -ie^{-i\theta_i} & ie^{i\theta_i} \end{pmatrix}$.

Introduce the sum and subtraction basis:

$$\hat{x}_\pm = \frac{\hat{x}_s \pm \hat{x}_i}{\sqrt{2}}, \quad \hat{y}_\pm = \frac{\hat{y}_s \pm \hat{y}_i}{\sqrt{2}} \tag{31}$$

and we obtain the fluctuation vector

$$\delta\hat{X}_\pm = \left(\delta\hat{y}_+, \delta\hat{x}_+, \delta\hat{y}_-, \delta\hat{x}_-\right)^{\mathrm{T}} = Q\left(\delta\hat{x}_s, \delta\hat{x}_i, \delta\hat{y}_s, \delta\hat{y}_i\right)^{\mathrm{T}} \tag{32}$$

where $\mathrm{Q} = \frac{1}{\sqrt{2}}\begin{pmatrix} 0 & 0 & 1 & 1 \\ 1 & 1 & 0 & 0 \\ 0 & 0 & 1 & -1 \\ 1 & -1 & 0 & 0 \end{pmatrix}$.

The spectral noise density matrix $S_{\hat{X}_\pm}(\omega)$ is calculated by:

$$S_{\hat{X}_\pm}(\omega) = \left\langle \delta\hat{X}_\pm(\omega)\delta\hat{X}_\pm^{\mathrm{T}}(-\omega)\right\rangle = Q \cdot P \cdot S_a(\omega) \cdot (Q \cdot P)^{\mathrm{T}} \tag{33}$$

where $S_a(\omega)$ is defined in Equation(24).

The Duan criterion has the following form:[52]

$$C_s = (\Delta\hat{x}_-)^2 + (\Delta\hat{y}_+)^2 - |G| \geq 0 \tag{34}$$

where $(\Delta\hat{x}_-)^2 = S_{\hat{X}_\pm}(\omega)(4,4)$, $(\Delta\hat{y}_+)^2 = S_{\hat{X}_\pm}(\omega)(1,1)$, and $G = \cos(\theta_s - \theta_i)$. If the Duan criterion is not satisfied, i.e., $C_s < 0$, the bipartite modes exhibit entanglement. A reduced value of C_s signifies an enhanced degree of quantum entanglement.

The condition for optimizing the entanglement degree, as determined through simulation, corresponds to the optimal quadrature of the signal mode's single-mode squeezed state, which simultaneously minimizes quantum back-action noise to the maximal extent. Hence, this EPR-entangled quantum optical frequency comb (QFC) platform can be harnessed to effectuate substantial noise attenuation.

As illustrated in **Figure 5**, the signal and idler beams manifest EPR-entangled sidebands. Initially, the quantum statistics of both beams adhere to a thermal state distribution, resulting in substantial quantum noise. However, by detecting the idler beam at a specific angle θ_i, the quantum statistics of the signal beam undergo instantaneous squeezing at an angle $-\theta_i$,[20] facilitating the bypassing of SQL. We introduce the readout angle $\varphi = \theta_s - \theta_i$, which provides a framework for further probing frequency-dependent squeezing through EPR entanglement, specifically in relation to the readout angle and observation frequency.

4. Entanglement and Squeezing Analysis

In this section, we undertake a thorough investigation of signal-idler two-mode entanglement, leveraging simulation results derived from practical parameters. By utilizing the two-mode squeezed state, we generate a single-mode squeezed state in the signal mode, subsequently analyzing its frequency-dependent squeezing characteristics. Furthermore, a comparative analysis is conducted to evaluate the entanglement properties under both normal and anomalous dispersion conditions.

4.1. Simulation Process

The primary computational tool employed in this section is Wolfram Mathematica, which operates under a temperature gradient of $\Delta T = 80\,^{\circ}\mathrm{C}$, thereby ensuring the simulation temperature T is sustained at $100\,^{\circ}\mathrm{C}$. The simulation procedure unfolds as follows: First, the structural parameters of the microring resonator are delineated to model the effective refractive index $n_{\mathrm{eff}}(\omega)$. Next, the central frequency of the pump light ($\Omega_0 \approx 1.21 \times 10^{15}$ rads^{-1}) is determined, followed by the calculation of the resonance mode and the dispersion parameter D_{int}. The subsequent phase entails modeling the coupling interactions between the microring resonator and the bus waveguide, which facilitates the extraction of pivotal parameters such as the coupling coefficient κ_{ex}. Finally, the entanglement between the signal and idler modes is rigorously evaluated using the criterion $C_s < 0$, and a detailed exploration of frequency-dependent squeezing is conducted. As the comb generation process nears the threshold of the optical parametric oscillator (OPO), the linearization approach discussed in Section 3 becomes insufficient, as higher-order fluctuations impose a considerable impact on the entanglement characteristics.[53,54] Consequently, the entanglement analysis presented in this section is confined to conditions well removed from the threshold. Ultimately, we investigate the interplay between the quality factor–comprising both the intrinsic quality factor Q_0 and the loaded quality factor Q–and the entanglement bandwidth and threshold power.

4.2. EPR Entangled QFCs

Utilizing our design platform, we have successfully generated EPR-entangled frequency combs comprising 12 channels (equivalent to 6 pairs), as demonstrated in **Figure 6**. In the case of anomalous dispersion, we set $\sigma_c = 8\,\mathrm{GHz}$, whereas for normal dispersion, $\sigma_c = 18\,\mathrm{GHz}$. Furthermore, our QFC operates under the effects of hysteresis, as detailed in refs. [35, 55]

In Figure 6, the S-shaped brown curve depicts the frequency modes below the OPO threshold, where the spontaneous FWM process is governed by vacuum fluctuations. In contrast, the vibrant bifurcation structure represents the modes above the OPO threshold, where the pump signal is sufficiently intense to induce coherent interactions via stimulated FWM. Panel (a) of Figure 6 illustrates the scenario of anomalous dispersion, while panel (b) presents the case of normal dispersion.

For the case of $l = 4$, the solutions to Equation (20) are depicted in **Figure 7**. In stages I and IV, the orange and red curves denote conditions where the system remains below the OPO threshold, resulting in null amplitudes for both the signal and idler modes. During these stages, only the amplitude of the pump mode is modulated by the injected pump power, signifying that the system's dynamics are predominantly governed by the pump in steady-state conditions. Conversely, stages II and III, represented by the blue and green curves, correspond to scenarios where the system exceeds the OPO threshold. In these stages, the amplitudes of all intracavity modes exhibit a heightened sensitivity to variations in the pump power, underscoring the nonlinear characteristics of the system. The intricate interactions between the intracavity modes and the injected pump mode are elaborated upon in ref. [49]. Additionally, a gray curve delineates regions below the OPO threshold, corresponding to unstable solutions, which are excluded from our simulation analysis due to their inherent instability.

The six pairs of EPR-entangled modes that we have generated are all conducive to entanglement analysis. However, in light of the similarity of the results across various modes, we will concentrate our investigation on the fourth and third modes ($l = 4$ and $l = 3$) for greater clarity. These modes can be delineated into four discrete stages, as illustrated in **Figures 8a** and **9a**. Stages I and IV correspond to a QFC operating sub-threshold, where bistability emerges, implying that each stage can stabilize into divergent states depending on the detuning process applied. In contrast, stages II and III correspond to a QFC operating above the threshold. By fine-tuning the angles θ_s and θ_i to identify the inflection point of C_s, we can comprehensively chart the entanglement distribution within the QFC.

The entanglement distribution as a function of the injected pump amplitude A^{in} and observation frequency f is depicted in Figures 8b and 9b, with a coupling rate of $r = 1.222$ and a pump detuning of $\sigma_c = 8$ GHz for anomalous dispersion. Similarly, Figures 8c and 9c illustrate the four stages under normal dispersion, and the corresponding entanglement distribution is shown in Figures 8d and 9d, maintaining the same coupling rate of $r = 1.222$ and a pump detuning of $\sigma_c = 18$ GHz. Our observations reveal that an increase in the injected pump amplitude leads to a higher peak in the entanglement degree during stage I. The simulation results also show that stages I and IV exhibit

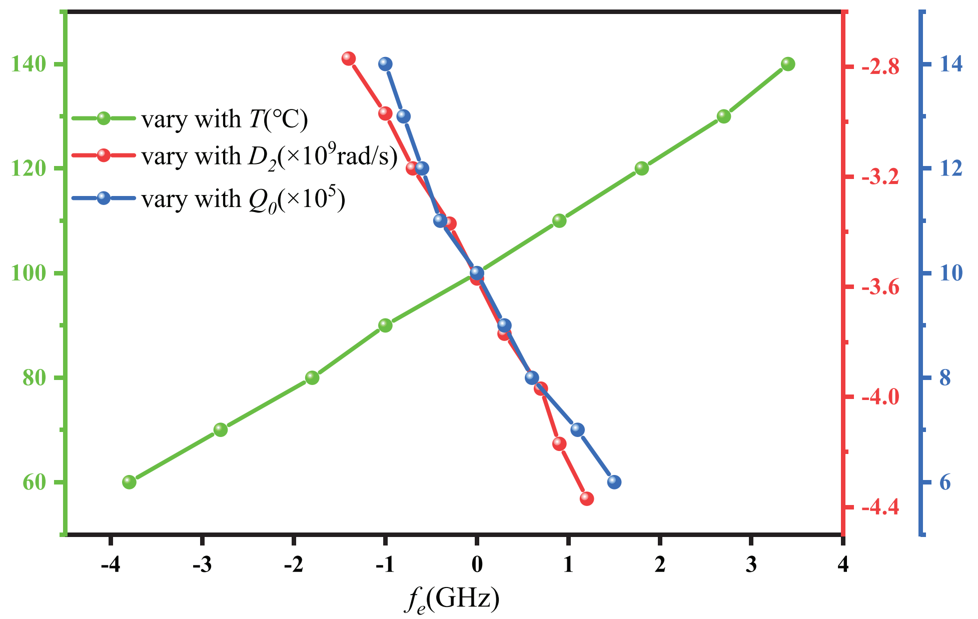

Figure 11. The graph depicts the relationship between the offset frequency f_e and three factors: temperature T, second-order dispersion coefficient D_2, and intrinsic quality factor Q_0. For each analysis, only one parameter is varied while the others are maintained at their ideal values. The three curves converge at the point where $f_e = 0$, signifying the conditions under which all parameters are at their optimal values.

a single minimum, while stages II and III have two distinct minima. Comparing the entanglement distribution patterns for anomalous and normal dispersion indicates that, under normal dispersion, the optimal observation frequency tends to shift upward. By fine-tuning the injected pump amplitude and observation frequency, it is possible to achieve maximum entanglement and significant noise suppression.

4.3. Frequency-Dependent Squeezing

To replace narrowband filter cavities and achieve a cost-effective and efficient implementation of frequency-dependent squeezing, we can leverage the six two-mode squeezed states generated in the previous simulation to prepare a single-mode squeezed state in the signal mode (simulation results are presented for $l = 4$). In the context of frequency-dependent squeezing, low frequencies predominantly exhibit amplitude squeezing, whereas high frequencies display phase squeezing. By detecting the idler mode at an angle θ_i, the signal mode is simultaneously squeezed at an angle $-\theta_i$. The interplay between the entanglement degree C_s, observation frequency f, and the readout angle ϕ (as illustrated in **Figure 10**) facilitates the quantification of frequency-dependent squeezing. For each observation frequency, the corresponding optimal readout angle can be determined.

To augment the practical applicability of the simulation model, we incorporated parameter deviations under non-ideal conditions and assessed their effects on the simulation outcomes, using the normal dispersion scenario as a representative example. The parameters considered include temperature (T), intrinsic quality factor (Q_0), and the second-order dispersion coefficient (D_2). Extensive simulations indicate that these deviations primarily result in shifts in the observation frequency, while leaving the core characteristics largely unchanged, as demonstrated in Figures 10c,d. To quantitatively assess the impact of these deviations under realistic conditions, we introduced a frequency offset (f_e) to represent the induced frequency shift, with positive values denoting a rightward shift and negative values indicating a leftward shift, as shown in **Figure 11**.

The silicon nitride microring resonator, distinguished by its integrated architecture, merges compactness with exceptional performance, positioning it as an exemplary candidate for cutting-edge applications. This investigation not only augments the sensitivity of displacement sensors, such as gravitational wave detectors, but also propels the advancement of quantum precision measurement technologies to new frontiers.

4.4. Entanglement Bandwidth and Threshold Power

In this subsection, we will highlight the differences between anomalous dispersion and normal dispersion.

First, we explore the relationship between the intrinsic quality factor Q_0, entanglement bandwidth δf, and threshold power P_{th}. **Figure 12** illustrates the curves under both anomalous and normal dispersion conditions. The results indicate that, within a suitable range, Q_0 is inversely proportional to the entanglement bandwidth δf and positively correlated with the threshold power P_{th}. Furthermore, as Q_0 increases, a slight increase in the entanglement extremum is observed. The loaded quality factor Q exhibits a relationship with both the entanglement bandwidth and the threshold power that parallels the behavior of the intrinsic quality factor Q_0. In this study, the coupling rate is fixed at $r = 1.222$. For the entanglement bandwidth calculation, we use a mode number of 4, with specified pump amplitude A^{in} and detuning. The fourth stage is chosen to best represent the entanglement bandwidth, and the $1/e$ of the entanglement extremum is used as the boundary, where e represents the natural constant.

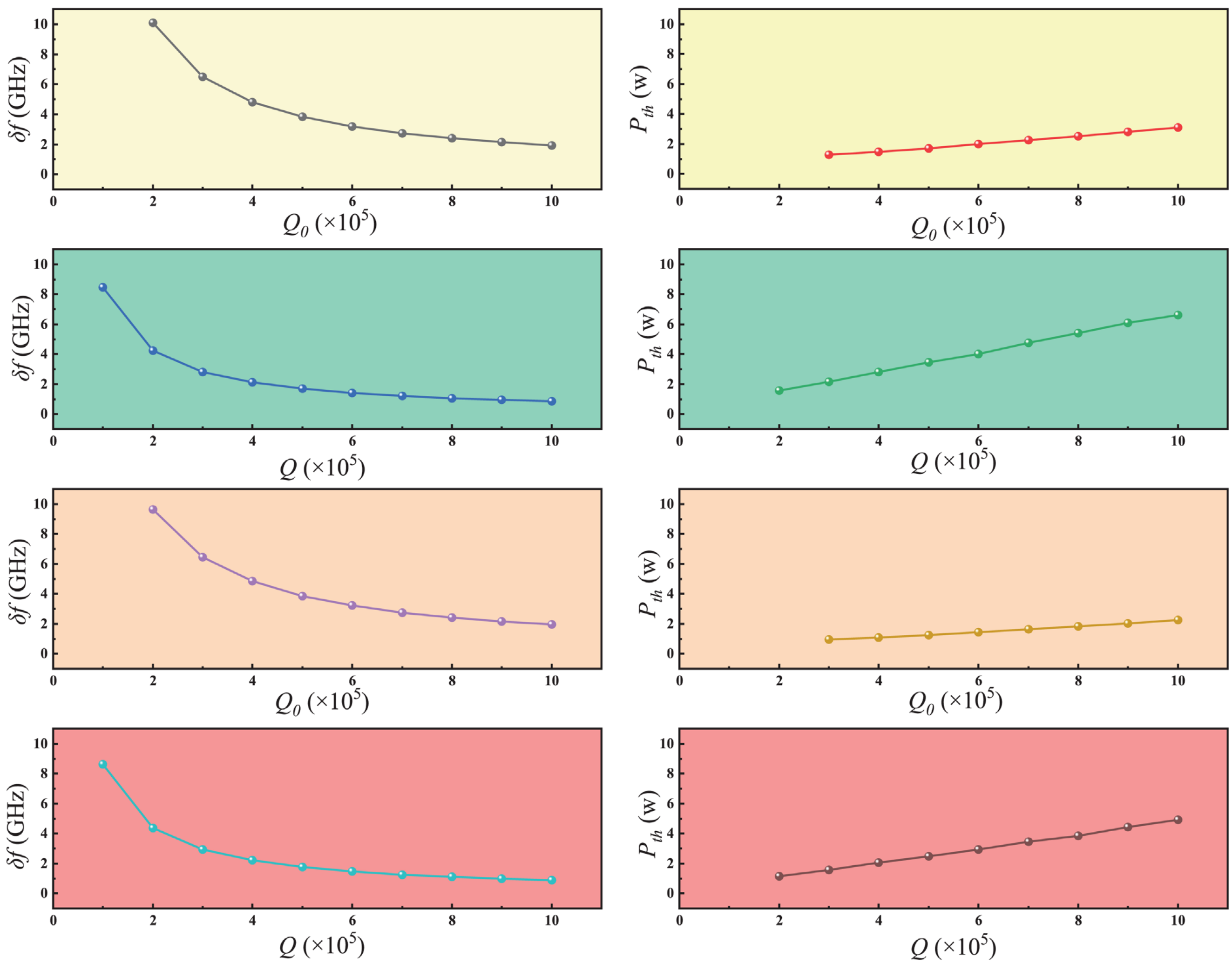

Figure 12. The relationship curve between the quality factor (including both the intrinsic quality factor Q_0 and the loaded quality factor Q), the entanglement bandwidth δf, and the threshold power P_{th}. The yellow graph depicts the relationship between Q_0, δf, and P_{th} under anomalous dispersion (σ_c = 3 GHz, r=1.222), while the green graph shows the corresponding relationship for Q, δf, and P_{th} in the same dispersion regime. The orange graph illustrates this relationship under normal dispersion for Q_0, δf, and P_{th}, and the red graph presents the same for Q, δf, and P_{th} under normal dispersion (σ_c = 3 GHz, r=1.222).

It can be observed that, for equivalent quality factors and detuning, the threshold power for normal dispersion is marginally inferior to that for anomalous dispersion. This disparity stems from the fact that, in our simulations, the nonlinear coefficient η_1 for normal dispersion surpasses η_2 for anomalous dispersion ($\eta_1 = 27.75$, $\eta_2 = 20.93$). Consequently, normal dispersion engenders more substantial nonlinear effects for the same optical power, thereby necessitating a reduced threshold power.

In contrast to the threshold power required for the initial comb tooth to emerge,[55] the threshold power discussed here pertains to the minimum pump power needed to generate comb teeth corresponding to a specific mode number (with $l = 1$ selected for this study). As Q_0 increases, the resonance peaks in Figure 3 become progressively narrower, while the detuning remains fixed, thereby hindering the growth of comb teeth for this particular mode number. Consequently, a higher threshold power is necessitated.

5. Conclusion

In summary, we have developed a robust platform for designing EPR-entangled QFCs utilizing a silicon nitride microring resonator. This platform leverages the bipartite entanglement criterion to investigate how the resonator's structural parameters influence the degree of entanglement. Our QFC is capable of generating at least 12 channels of quantum-entangled states, positioning it as a promising candidate for multi-channel quantum information networks. We meticulously align various microcavity structures with distinct dispersions, performing an exhaustive analysis of the entanglement bandwidth and threshold power under both normal and anomalous dispersion conditions. Moreover, by utilizing one of the six EPR-entangled pairs generated, we engineer a frequency-dependent single-mode squeezed state, enabling the exploration of the intricate relationship between the readout angle and observation frequency. This provides valuable insights into frequency-dependent squeezing. Our findings demonstrate substantial potential for advancing quantum precision measurement applications.

Acknowledgements

This work was supported by the Key-Area Research and Development Program of Guangdong Province (Grant No.2018B030325002), the National Natural Science Foundation of China (Grant No.62075129, 61975119), the Open Project Program of SJTU-Pinghu Institute of Intelligent Optoelectronics (Grant No.2022SPIOE204) and the Sichuan Provincial Key Laboratory of Microwave Photonics (Grant 2023-04).

Conflict of Interest

The authors declare no conflict of interest.

Data Availability Statement

The data that support the findings of this study are available from the corresponding author upon reasonable request.

Keywords

bipartite entanglement criterion, dispersion, EPR entanglement, frequency-dependent squeezing, quality factor, silicon nitride microring resonators

Received: October 3, 2024
Revised: December 7, 2024
Published online:

[1] H. Yu, L. McCuller, M. Tse, N. Kijbunchoo, L. Barsotti, N. Mavalvala, (LIGO Scientific Collaboration), *Nature* **2020**, *583*, 43.
[2] F. Acernese, M. Agathos, L. Aiello, A. Allocca, A. Amato, S. Ansoldi, S. Antier, M. Arene, N. Arnaud, (The Virgo Collaboration), *Phys. Rev. Lett.* **2019**, *123*, 231108.
[3] C. M. Caves, *Phys. Rev. D* **1981**, *23*, 1693.
[4] D. F. Walls, *Nature* **1983**, *306*, 141.
[5] G. Breitenbach, S. Schiller, J. Mlynek, *Nature* **1997**, *387*, 471.
[6] R. Schnabel, *Phys. Rep.* **2017**, *684*, 1.
[7] T. L. S. Collaboration, *Nat. Phys.* **2011**, *7*, 962.
[8] T. L. S. Collaboration, *Nat. Photonics* **2013**, *7*, 613.
[9] H. J. Kimble, Y. Levin, A. B. Matsko, K. S. Thorne, S. P. Vyatchanin, *Phys. Rev. D* **2001**, *65*, 022002.
[10] S. Chelkowski, H. Vahlbruch, B. Hage, A. Franzen, N. Lastzka, K. Danzmann, R. Schnabel, *Phys. Rev. A* **2005**, *71*, 013806.
[11] F. Y. Khalili, *Phys. Rev. D* **2010**, *81*, 122002.
[12] L. Barsotti, J. Harms, R. Schnabel, *Rep. Prog. Phys.* **2018**, *82*, 016905.
[13] S. Vyatchanin, E. Zubova, *Phys. Lett. A* **1995**, *201*, 269.
[14] V. B. Braginsky, Y. I. Vorontsov, K. S. Thorne, *Science* **1980**, *209*, 547.
[15] G. Vasilakis, H. Shen, K. Jensen, M. Balabas, D. Salart, B. Chen, E. S. Polzik, *Nat. Phys.* **2015**, *11*, 389.
[16] J. B. Hertzberg, T. Rocheleau, T. Ndukum, M. Savva, A. A. Clerk, K. C. Schwab, *Nat. Phys.* **2010**, *6*, 213.
[17] J. Suh, A. J. Weinstein, C. U. Lei, E. E. Wollman, S. K. Steinke, P. Meystre, A. A. Clerk, K. C. Schwab, *Science* **2014**, *344*, 1262.
[18] I. Shomroni, L. Qiu, D. Malz, A. Nunnenkamp, T. J. Kippenberg, *Nat. Commun.* **2019**, *10*, 2086.
[19] Y. Chen, S. L. Danilishin, F. Y. Khalili, H. Müller-Ebhardt, *General Relativity and Gravitation* **2011**, *43*, 671.
[20] Y. Ma, H. Miao, B. H. Pang, M. Evans, C. Zhao, J. Harms, R. Schnabel, Y. Chen, *Nat. Phys.* **2017**, *13*, 776.
[21] M. J. Yap, P. Altin, T. G. McRae, B. J. J. Slagmolen, R. L. Ward, D. E. McClelland, *Nat. Photonics* **2020**, *14*, 223.
[22] J. Südbeck, S. Steinlechner, M. Korobko, R. Schnabel, *Nat. Photonics* **2020**, *14*, 240.
[23] H. Vahlbruch, S. Chelkowski, B. Hage, A. Franzen, K. Danzmann, R. Schnabel, *Phys. Rev. Lett.* **2006**, *97*, 011101.
[24] S. S. Y. Chua, M. S. Stefszky, C. M. Mow-Lowry, B. C. Buchler, S. Dwyer, D. A. Shaddock, P. K. Lam, D. E. McClelland, *Opt. Lett.* **2011**, *36*, 4680.
[25] J. Junker, D. Wilken, N. Johny, D. Steinmeyer, M. Heurs, *Phys. Rev. Lett.* **2022**, *129*, 033602.
[26] U. Leonhardt, *Measuring the Quantum State of Light*, Cambridge University Press, Cambridge, England **1997**.
[27] K. Wu, Q. Zhang, A. W. Poon, *Opt. Express* **2021**, *29*, 24750.
[28] V. D. Vaidya, B. Morrison, L. Helt, R. Shahrokshahi, D. Mahler, M. Collins, K. Tan, J. Lavoie, A. Repingon, M. Menotti, N. Quesada, R. C. Pooser, A. E. Lita, T. gerrits, S. W. Nam, Z. Vernon, *Sci. Adv.* **2020**, *6*, eaba9186.
[29] J. Chen, Z. H. Levine, J. Fan, A. L. Migdall, *Opt. Express* **2011**, *19*, 1470.
[30] W. Wen, Z. Chen, L. Lu, W. Yan, W. Xue, P. Zhang, Y. Lu, S. Zhu, X. S. Ma, *Phys. Rev. Appl.* **2022**, *18*, 024059.
[31] W. Wen, W. Yan, C. Lu, L. Lu, X. Wu, Y. Lu, S. Zhu, X. S. Ma, *Phys. Rev. Appl.* **2023**, *20*, 064032.
[32] W. Asavanant, A. Furusawa, *Phys. Rev. A* **2024**, *109*, 040101.
[33] X. Chen, Z. Fu, Q. Gong, J. Wang, *Adv. Photonics* **2021**, *3*, 064002.
[34] A. Tikan, J. Riemensberger, K. Komagata, S. Hönl, M. Churaev, C. Skehan, H. Guo, R. N. Wang, J. Liu, P. Seidler, T. J. Kippenberg, *Nat. Phys.* **2021**, *17*, 604.
[35] N. Li, B. Ji, Y. Shen, G. He, *Phys. Rev. Appl.* **2024**, *21*, 054058.
[36] J. M. Dudley, G. Genty, S. Coen, *Rev. Mod. Phys.* **2006**, *78*, 1135.
[37] H. Shi, Z. Chen, S. E. Fraser, M. Yu, Z. Zhang, Q. Zhuang, *npj Quantum Inf.* **2023**, *9*, 91.
[38] C. Godey, I. V. Balakireva, A. Coillet, Y. K. Chembo, *Phys. Rev. A* **2014**, *89*, 063814.
[39] A. Arbabi, L. L. Goddard, *Opt. Lett.* **2013**, *38*, 3878.
[40] G. Huang, E. Lucas, J. Liu, A. S. Raja, G. Lihachev, M. L. Gorodetsky, N. J. Engelsen, T. J. Kippenberg, *Phys. Rev. A* **2019**, *99*, 061801.
[41] Z. Vernon, J. E. Sipe, *Phys. Rev. A* **2015**, *91*, 053802.
[42] Z. Vernon, J. E. Sipe, *Phys. Rev. A* **2015**, *92*, 033840.
[43] B. Ji, N. Li, G. He, *arXiv* **2024**, *2406.16622*.
[44] U. A. Javid, R. Lopez-Rios, J. Ling, A. Graf, J. Staffa, Q. Lin, *Nat. Photonics* **2023**, *17*, 883.
[45] H. Zeng, Z.-Q. He, Y.-R. Fan, Y. Luo, C. Lyu, J. P. Wu, Y. B. Li, S. Liu, D. Wang, D. C. Zhang, J. J. Zeng, G. W. Deng, Y. Wang, H. Z. Song, Z. Wang, L. X. You, K. Guo, C. Z. Sun, Y. Luo, G. C. Guo, Q. Zhou, *Phys. Rev. Lett.* **2024**, *132*, 133603.
[46] Y. Wang, W. Zhang, Q. Wang, X. Feng, X. Liu, J. Peng, *Opt. Lett.* **2004**, *29*, 889.
[47] Y. K. Chembo, *Phys. Rev. A* **2016**, *93*, 033820.
[48] S. J. Whalen, H. J. Carmichael, *Phys. Rev. A* **2016**, *93*, 063820.
[49] A. B. Matsko, A. A. Savchenkov, D. Strekalov, V. S. Ilchenko, L. Maleki, *Phys. Rev. A* **2005**, *71*, 033804.

[50] L.-M. Duan, G. Giedke, J. I. Cirac, P. Zoller, *Phys. Rev. Lett.* **2000**, *84*, 2722.
[51] D. Wang, Q. Wang, Q. Zhang, Y. Li, *J. Opt. Soc. Am. B* **2023**, *40*, 3.
[52] C. González-Arciniegas, N. Treps, P. Nussenzveig, *Opt. Lett.* **2017**, *42*, 4865.
[53] E. Ng, R. Yanagimoto, M. Jankowski, M. M. Fejer, H. Mabuchi, *arXiv:2307.05464* **2023**.
[54] C. Vendromin, Y. Liu, Z. Yang, J. E. Sipe, *arXiv:2404.15563* **2024**.
[55] Y. K. Chembo, N. Yu, *Phys. Rev. A* **2010**, *82*, 033801.